AGU ADVANCING EARTH AND SPACE SCIENCE

JGR Earth Surface

RESEARCH ARTICLE
10.1029/2022JF006870

Bi-Linear Laws Govern the Impacts of Debris Flows, Debris Avalanches, and Rock Avalanches on Flexible Barrier

Yong Kong[1], Mingfu Guan[1], Xingyue Li[2], Jidong Zhao[3], and Haochen Yan[1]

[1]Department of Civil Engineering, The University of Hong Kong, Hong Kong SAR, China, [2]Department of Geotechnical Engineering, College of Civil Engineering, Tongji University, Shanghai, China, [3]Department of Civil and Environmental Engineering, The Hong Kong University of Science and Technology, Hong Kong SAR, China

Key Points:

- We present numerical measures of the impact loads of debris flows/avalanches and rock avalanches on a flexible ring net barrier system
- Bi-linear laws relate peak impact to Fr, peak cable force, or maximum barrier deformation with turning points due to shifts of dead zones
- Flow materials and dynamics jointly control the obtained bi-linear laws, which underpin widely used analytical and simplified solutions

Supporting Information:

Supporting Information may be found in the online version of this article.

Correspondence to:

M. Guan,
mfguan@hku.hk

Citation:

Kong, Y., Guan, M., Li, X., Zhao, J., & Yan, H. (2022). Bi-linear laws govern the impacts of debris flows, debris avalanches, and rock avalanches on flexible barrier. *Journal of Geophysical Research: Earth Surface*, *127*, e2022JF006870. https://doi.org/10.1029/2022JF006870

Received 9 AUG 2022
Accepted 28 OCT 2022

Abstract Geophysical mass flows impacting flexible barriers can create complex flow patterns and multiway solid-fluid-structure interactions, wherein estimates of impact loads rely predominantly on analytical or simplified solutions. However, an examination of the fundamental relations, applicability, and underlying mechanisms of these solutions has been so far elusive. Here, using a coupled continuum-discrete method, we systematically examine the physical laws of multiphase, multiway interactions between geophysical flows of variable natures, and a permeable flexible ring net barrier system. This model well captures the essential physics observed in experiments and field investigations. Our results reveal for the first time that unified bi-linear laws underpin widely used analytical and simplified solutions, with inflection points caused by the transitions from trapezoid-shaped to triangle-shaped dead zones. Specifically, the peak impact load increases bi-linearly with increasing Froude number, peak cable force, or maximum barrier deformation. Flow materials (wet vs. dry) and impact dynamics (slow vs. fast) jointly drive the patterns of identified bi-linear correlations. These findings offer a physics-based, significant improvement over existing solutions to impact problems for geophysical flows.

Plain Language Summary Flexible barriers are increasingly used worldwide to mitigate debris flows, debris/rock/snow avalanches, and rockfalls. Although many methods exist to estimate critical design factors of flexible barriers, a systematic examination of their applicability and underlying relations remains elusive. The status quo has been largely caused by the challenges of capturing and quantifying the multiphase, multiway flow-barrier interactions. Here, we perform a series of hybrid solid-fluid simulations to explore the impact of debris flows/avalanches and rock avalanches on a flexible barrier system. Our numerical predictions of critical physical processes show reasonable consistency with experimental and field observations. For the first time, the physics-based numerical measures of the flow-barrier forces, in-barrier forces, and barrier load-deformation relations reveal the unified bi-linear laws behind widely used methods. We find that the flow-specific turning points of the bi-linear laws are due to the changes from trapezoid-shaped to triangle-shaped jammed regions formed upstream of the barrier. Our findings quantitatively explain how flow properties (e.g., wet vs. dry and slow vs. fast) control the obtained bi-linear laws. This study provides a crucial improvement over widely used methods for geohazard scientists and engineers to impact problems for geophysical flows.

1. Introduction

Geophysical mass flows are common phenomena in mountain regions worldwide, with the size, frequency, and hazardous potential of events predicted to increase due to extreme rainstorms, land-cover changes, and severe wildfires (Hoch et al., 2021; D. Li et al., 2022; Pisano et al., 2017). Compared with traditional rigid countermeasures (Hungr et al., 1984), flexible barriers are increasingly used to mitigate catastrophic geophysical flows (Figure S1 in Supporting Information S1), such as debris flows, debris/rock/snow avalanches, and rockfalls (Caviezel et al., 2021; Cook et al., 2021; Iverson et al., 2011; Trottet et al., 2022). A fundamental issue in hazard mitigation is determining the total impact load of geophysical flows on a flexible barrier. However, this total impact load was not directly measurable in physical experiments before (e.g., Bugnion et al., 2012; DeNatale et al., 1999; Vicari et al., 2021). Furthermore, impact loads of fluid and solid materials in a geophysical flow on a rigid obstacle can be separated from the measured impact pressure signals (Cui et al., 2015; Zheng et al., 2022), while a physical measurement for flexible barriers identifying the contribution of individual phases to the total impact remains elusive. The difficulty is rooted in capturing and quantifying the multiphase, multiway flow-barrier interactions,

where many mechanisms governing energy and force can work simultaneously. A proper understanding of such an impact process and its physical laws is thus of profound scientific and engineering importance.

Estimating the peak impact of geophysical flows on flexible barriers for practical designs relies primarily on analytical solutions, including hydrostatic, hydrodynamic and hybrid models (Berger et al., 2021; Kwan & Cheung, 2012; Lam et al., 2022; see Appendix A). They require theoretical functions and empirical coefficients in conjunction with the Froude number (Fr) of impinging flows, which have been investigated in extensive studies (Kong et al., 2022; Li, Zhao, & Soga, 2021; Song et al., 2021). Fundamentally, calibrations of these Fr-related analytical solutions and their empirical coefficients depend upon the impact loads estimated in physical tests using simplified solutions (e.g., Song et al., 2022; Tan et al., 2019; Wang et al., 2022). For example, the cable-based solution (Ferrero et al., 2015; Ng et al., 2017) calculates the total impact load exerted on a flexible barrier by summing the normal impact forces on all its horizontal supporting cables. This solution converts the cable tensile force to the impact load normal to the barrier face and has been widely adopted in experiments (e.g., Lam et al., 2022; Song et al., 2022; Vicari et al., 2021). The spring solution applies Hooke's Law to estimate the impact load acting on a flexible barrier, using an equivalent barrier stiffness and the maximum barrier deflection in the flow direction. It has been investigated by flume and field tests (e.g., Ashwood & Hungr, 2016; Song et al., 2019; Wendeler, 2016). However, these simplified solutions feature idealized assumptions and lack scrutiny (details provided in Appendix A), and a systematic examination of their applicability and underlying relations is still elusive. A limited understanding of the physical laws behind widely used analytical and simplified solutions hampers effective hazard mitigation regarding flexible barriers.

Besides physical experiments and theoretical analysis, many numerical methods have been applied to investigate the impacts of geophysical flows on flexible barriers, such as mesh-free methods (smoothed particle hydrodynamics [SPH], Fávero Neto et al., 2020; Material Point Method, Vicari et al., 2022; discrete element method [DEM], Albaba et al., 2017), grid-dependent methods (finite element method [FEM], Brighenti et al., 2013), and coupled frameworks (SPH-DEM-FEM, B. Li, Wang, et al., 2021; DEM-FEM, Liu et al., 2020; computational fluid dynamics [CFD] coupled with DEM, Kong, Li, et al., 2021; Lattice Boltzmann Method coupled with DEM and FEM, Leonardi et al., 2016; CFD-FEM, Von Boetticher et al., 2011). Nonetheless, simplifications of flow dynamics and flexible barriers have prevented a deeper understanding of the underlying relations and mechanisms of the flow-barrier interactions. On the one hand, the solid-fluid nature of a geophysical flow plays a crucial role in predicting its propagation and impact (De Haas et al., 2021; Iverson, 1997; Pudasaini & Mergili, 2019) but has commonly been modeled as pure continuum or granular flows (Albaba et al., 2017; Liu et al., 2020; Von Boetticher et al., 2011). On the other hand, permeable flexible barrier systems (Figure 1a) are simulated as membranes (Leonardi et al., 2016; Vicari et al., 2022), and net units are generated in a 2D plane (Brighenti et al., 2013; Kong, Li, et al., 2021; B. Li, Wang, et al., 2021) by ignoring the cable-ring-ring slidings in a 3D space. However, these omitted in-flow multiphase and in-barrier multiway interactions are essential for accurately predicting systematic structure deformations, evolving load sharings and distributions, and thus peak barrier load.

This study will focus on scrutinizing three fundamental relationships for the Fr-related analytical (Figure 5a), cable-based (Figure 6), and spring (Figure 7e) solutions based on systematic numerical measures of the flow-barrier forces, in-barrier forces, and barrier load-deformation relations. The employed solid-fluid coupled model considers essential physics, including the in-flow multiphase and flow-barrier multiway interactions, materials passing through, and the cable-ring-ring slidings. The results can facilitate a unified description of the impacts and interpret the underlying physics when geophysical flows of variable natures impact a multicomponent flexible barrier system.

2. Methods

A unified CFD-DEM coupling approach is employed to probe the dynamics of geophysical flows of different natures impacting a flexible barrier. A flexible barrier is modeled by DEM (Figure 1a), while a typical debris flow is treated as a mixture of discrete particles and a continuous slurry by DEM and CFD (Figure 1d), respectively. The motions of a particle are governed by Newton's equations, and the fluid is controlled by the locally averaged Navier-Stokes equation for each fluid cell with the finite-volume method. The two-way coupling scheme offers a unified way to describe the solid-liquid interactions in a debris flow and between barrier components and debris liquid. This method has been widely applied to investigate granular-fluid systems

relevant to geomechanics (Breard et al., 2020; Li, Zhao, & Soga, 2021; Zhao & Shan, 2013) and industry (Goniva et al., 2012; Yu & Zhao, 2021). Recently, it has been extended to examine debris-flow impacts on flexible barriers (Kong et al., 2022; Kong, Li, et al., 2021; X. Li et al., 2020), where the modeling of different barrier components has been calibrated and verified. Key ingredients of this hybrid solid-fluid method can be found in Text S2 in Supporting Information S1.

2.1. Modeling Geophysical Flows Against Flexible Ring Net Barrier System

Figure 1a-upper shows a typical flexible barrier system composed of a ring net, brake elements, and cables used in New Zealand for arresting debris flows. It was fixed on three sides (left, bottom, and right) by anchors and nails driven into the ground. We model such a barrier by assembling 5 supporting cables, 10 brake elements, and a ring net consisting of 382 interlocking rings (Figure 1a-lower). The bottom cable and lateral edges of the top and middle cables are fixed to mimic the anchored boundaries. DEM is used to model all barrier components as nodal particles connected with parallel bonds (Potyondy & Cundall, 2004; Zhao & Crosta, 2018; see details in Text S3 in Supporting Information S1). For instance, interlocking rings are idealized as connected nodal particles placed at the physical nodes of rings (Figure 1b). Analogously, a cable is modeled with a set of nodal particles whose centers are along the rope, and a brake element is simplified as two nodal particles linked by a piecewise-linear bond (X. Li et al., 2020; Xu et al., 2018). Both ends of a horizontal supporting cable are equipped with two brake elements (Figure 1a), which are designed to dissipate impact energy and lengthen significantly under debris-flow impact. The locations of simulated brake elements have been visualized in Figure S2 (see Text S3 in Supporting

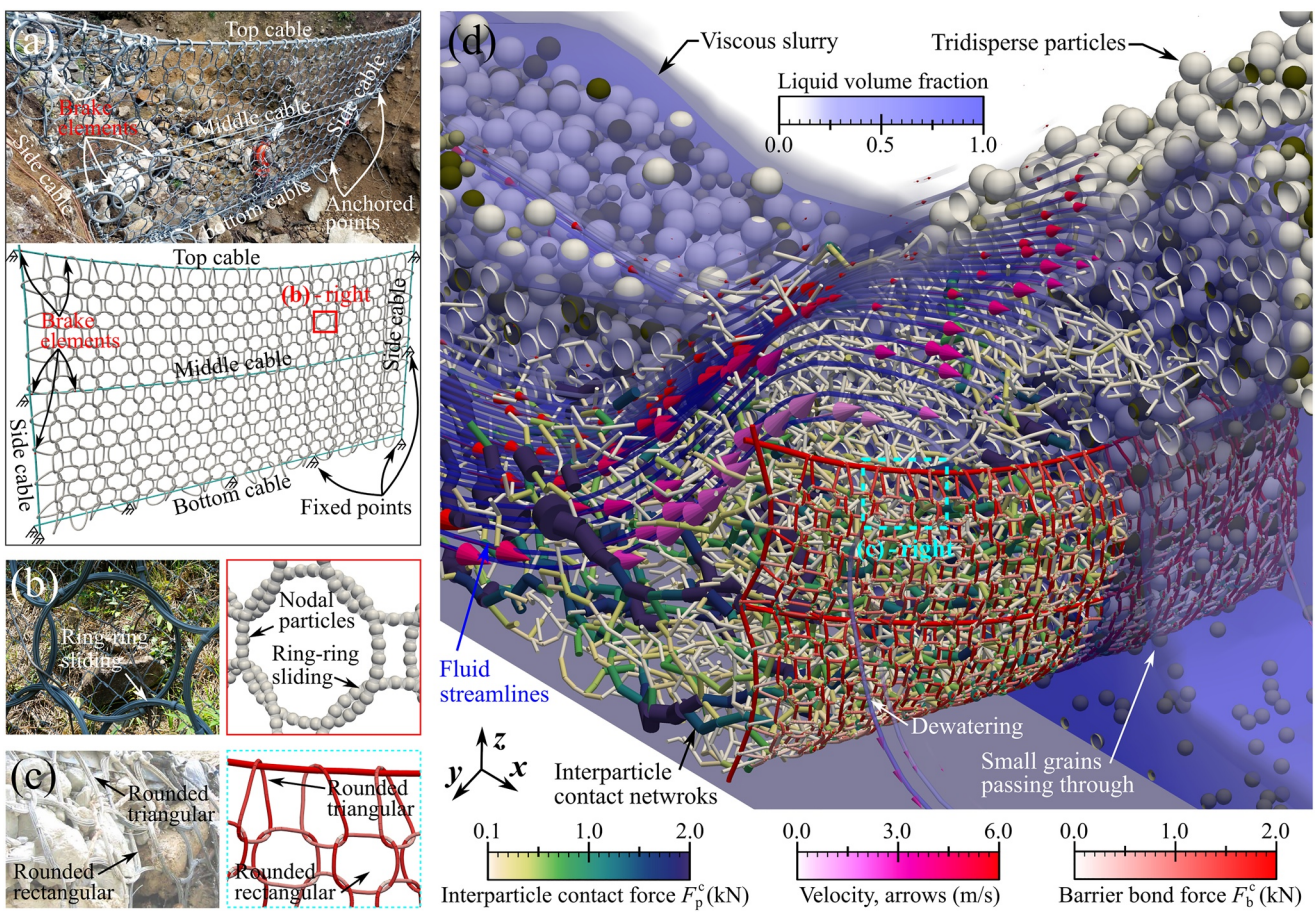

Figure 1. Undeformed and deformed flexible ring net barrier system. (a)–(c) present a comparison between field photos and numerical snapshots for the barrier, interlocking rings, and local deformation characteristics, respectively. (d) shows the simulated dynamics for a typical debris flow impacting the barrier, where split views display debris fluid and gap-graded particles (back half-space) as well as fluid streamlines and interparticle contacts (front half-space). Photos in (a) and (c) are modified from GEOVERT (2016) and Wendeler (2016), respectively.

Table 1
Summary of Key Parameters Used in the Multiphase Simulations

Items	Parameter [units]	Values
Particles in a flow	Particle number	28,125
	Density[a] [kg/m^3]	2,650
	Diameters [m]	0.04, 0.06, 0.08
	Young's modulus (particle-particle contact) [GPa]	70
	Young's modulus (particle-wall contact) [GPa]	700
	Poisson's ratio[a]	0.3
	Restitution coefficient[a]	0.4
	Interparticle friction coefficient	0.7
	Particle-wall friction coefficient	0.5
	Rolling friction coefficient	0.15
Particles in a barrier[b]	Diameter [m]	0.006
	Number	14,725
	Density for ring element, cable, brake [kg/m^3]	7,800, 12,000, 20,000
	Young's modulus [GPa]	10
	Poisson's ratio	0.3
	Restitution coefficient	0.1
	Friction coefficient	0.1
Bonds in a barrier[b]	Normal stiffness of ring element [N/m]	3×10^{11}
	Shear stiffness of ring element [N/m]	9×10^{8}
	Normal stiffness of cable [N/m]	8×10^{11}
	Shear stiffness of cable [N/m]	8×10^{8}
	Stiffnesses of the brake at the three stages [$\times 10^8$ N/m]	20, 1.3, 3.2
	Force limits of brake at the three stages [kN]	50, 80, 100
Air[a]	Density [kg/m^3]	1
	Viscosity [Pa · s]	1.48×10^{-5}
Fluid[c]	Density [kg/m^3]	1,350
	Consistency index [Pa · s^n]	21.30
	Flow index	0.24
	Yield stress [Pa]	17.86
Simulation control	Cell size [m]	0.15*0.15*0.15
	Timestep in DEM [s]	5×10^{-7}
	Timestep in CFD [s]	5×10^{-6}
	Simulated real-time [s]	2–12

[a]Refer to the typical values of physical properties for geophysical flows (Iverson, 1997). [b]Refer to key parameters in modeling a flexible ring net barrier (Dugelas et al., 2019; X. Li et al., 2020; Xu et al., 2018). [c]Refer to typical values of the non-Newtonian fluids in a debris flow (Remaître et al., 2005).

Information S1). Moreover, the total physical mass of the ring net and cables is assumed to be lumped over these nodal particles, according to which their density is adjusted (Dugelas et al., 2019; X. Li et al., 2020). Key parameters for modeling a flexible ring net barrier are summarized in Table 1, and the full model description, calibration, and validation can be found in X. Li et al. (2020).

Figure 1d demonstrates a typical debris flow impacting a flexible barrier (0.9-m-high, 1.8-m-wide) constructed on an inclined channel, capturing critical physical processes, such as flow retaining and climbing, the cable-ring-ring sliding, dewatering, and small particles passing through. In particular, Figure 1c-right demonstrates an enlarged view of the area marked by a dashed rectangular in Figure 1d. Figure 1c indicates that our model

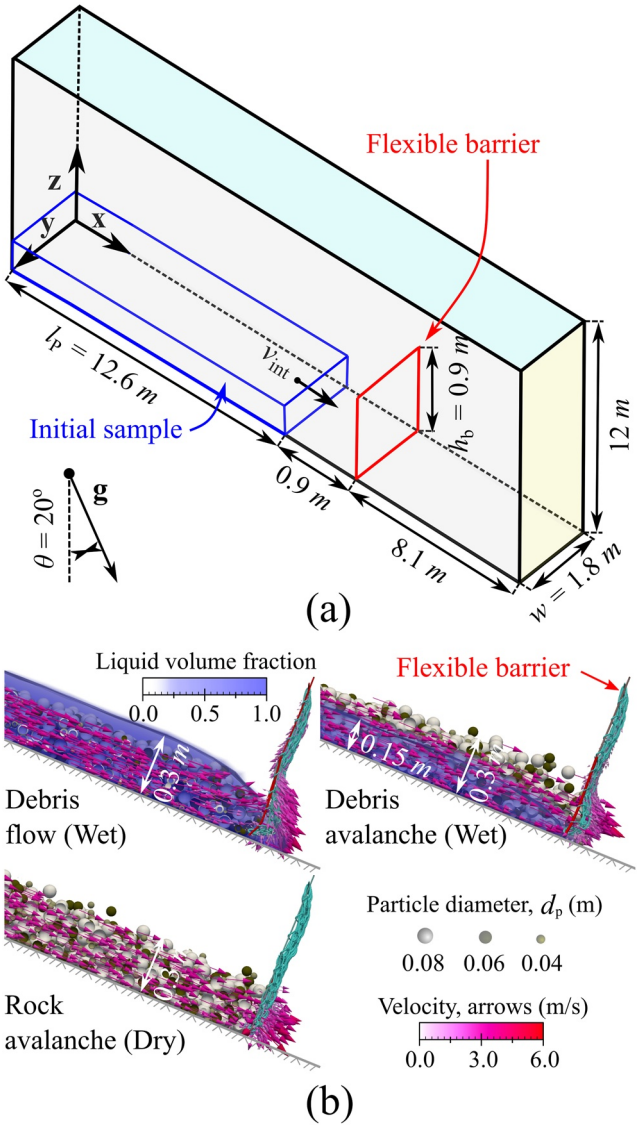

Figure 2. Model setup: (a) Model geometry before the release of initial sample and (b) Numerical snapshots of representative cases of debris flow, debris avalanche, and rock avalanche impacting a flexible ring net barrier at the frontal impact process.

captures the local deformations of barrier components and the intricate connections among interlocking rings and cables, where the cable-ring-ring frictional sliding and collision are enabled. Moreover, the interaction between debris particles and barrier nodal particles can be readily handled within the same DEM framework. Meanwhile, the interaction between debris fluid and barrier nodal particles can be considered the same as the fluid-particle interactions in a debris flow under the unified CFD-DEM method. As a result, we can obtain loads of solid particles and the viscous fluid in a geophysical mass flow acting on barrier nodal particles via interparticle contact forces and fluid-particle interaction forces, respectively.

2.2. Model Setup

Figure 2a illustrates the geometric model setup for a geophysical mass flow against a flexible barrier constructed on an inclined channel with a slope angle θ. In DEM, the sides and bottom of the flow channel are modeled as frictional rigid walls. An outlet face at the end of the channel, an upper atmosphere face, and four no-slip channel walls bound the CFD domain. Only fluid cells in a mixture sample are filled with viscous slurry at the initial state, leaving the rest of the CFD domain filled with air. Unlike water as the fluid phase (Fang et al., 2021; Zhou et al., 2020), viscous slurries in DFs/debris avalanches (DAs) are treated as the more complicated non-Newtonian fluid modeled with the Herschel-Bulkley model (Remaître et al., 2005). Although a fixed rheological formula cannot accurately predict debris-flow behavior (Iverson, 2003), the interstitial fluid in a debris-flow mixture can be best described by a Herschel-Bulkley model with shear thinning rheology (Coussot et al., 1998; Von Boetticher et al., 2016).

This study performs systematic simulations of debris flows (DFs), debris avalanches (DAs), and rock avalanches (RAs) against a flexible ring net barrier. A typical debris-flow sample is simulated as a mixture of tridisperse particles and a viscous slurry (Figure 2b). The mass percentages of the particles with diameters d_p of 0.08, 0.06, and 0.04 m are 70%, 15%, and 15%, respectively. We adopt the gap-graded tridisperse particle distribution instead of a more realistic distribution (e.g., Gaussian or Power-law) partially because it can provide an adequate sample volume for the complete impact process while maintaining affordable computational efficiency. The bulk volume of the sample (i.e., 6.8 m^3) is appropriate to maintain the overflow process with a reasonable duration in each simulation. Thus, increasing the released mass may not affect the core results in this study. Moreover, the samples, including the fluid and solid phases, are initially assigned with prescribed velocities (v_{int} = 0.5–14 m/s) before being released to flow down an inclined channel under gravity and further impacting the barrier. Consequently, a broad range of Fr (0.5–8.7) is produced with a constant pre-impact flow depth of ~0.3 m. Note that the hypothesis of a uniform vertical velocity profile at the initial state is unrealistic (Iverson, 1997; Redaelli et al., 2021), which may affect the impact process. Redaelli et al. (2021) reported that the impact load of dry granular flows on a rigid wall is negligibly affected by the shape of the velocity profile. In addition, compared to releasing a gravity-driven sample with prescribed initial velocities, using a continuous inflow of material (Pasqua et al., 2022) may produce a constant impact velocity of incoming flows and affect the Froude scaling on the flow-barrier interactions. As seen in Figure 2b, the initial heights of viscous slurries in DF, DA, and RA cases are set to 0.3, 0.15, and 0 m, respectively. Thus, the DF, DA, and RA cases can also be characterized as fully saturated, partially saturated, and dry granular flows, respectively. The total number of simulated particles in each simulation is 42,850 (28,125 in a flow and 14,725 in a barrier), with a maximum particle size ratio of ~13.3. Key adopted parameters and test scenarios are summarized in Tables 1 and 2, respectively.

Table 2
Numerical Test Scenarios

Group IDs	Debris flows (DFs)	Debris avalanches (DAs)	Rock avalanches (RAs)
v_{int} (m/s)	0.5, 1, 2, 3, 4, 6, 8, 10, 12, 14	0.5, 1, 2, 3, 4, 5, 6, 8, 10, 12, 14	1, 2, 3, 4, 5, 6, 8, 10, 12, 14
Fr	0.6–8.7	0.5–8.6	0.7–8.5

For each case, the computation time on an 8-core Intel CPU (3.7 GHz) desktop computer varies from 60 to 390 hr, primarily depending on the simulated flow materials (wet or dry) and real-time (2–12 s). Thus, instead of full-scale (10^1–10^2 m) ones, large-scale (10^0–10^1 m) simulations are conducted for computational efficiency. Furthermore, the adoptions of particle size distribution and barrier size are determined according to the scale of the setup in Figure 2a. On the one hand, the particle number along the flow width direction needs to be small enough to save computational cost and meanwhile sufficiently large to avoid boundary effect from the lateral walls. On the other hand, the barrier ring net size (i.e., ring diameter equal to 0.07 m) is determined to retain large particles (d_p = 0.08 m) in a flow while allowing small particles (d_p = 0.04 or 0.06 m) to pass through, which recovers the primary function of a real-world flexible barrier. In addition to solid volume concentrations and flow dynamics, the flow-barrier interactions can also be affected by the complex natures of geophysical flows, including varying flow depths (Faug et al., 2012; Iverson et al., 2016), broad particle size distributions (Cabrera & Estrada, 2021), large boulders (Belli et al., 2022; Piton et al., 2022), phase separation of the solid and fluid components (Leonardi et al., 2015; Pudasaini & Fischer, 2020), and erosion (Berger et al., 2011; Pudasaini & Krautblatter, 2021). Meanwhile, the barrier geometry and configuration (e.g., barrier width and height, number of horizontal supporting cables, and the ring-to-largest particle size ratio) may also affect the results presented in the following sections. These factors can be explored in the future.

Numerical predictions of key flow-barrier interactions and barrier deformations show reasonable consistency with experimental and field observations (Figures S3 and S4 in Supporting Information S1). Furthermore, each simulated flow type corresponds to distinct flow dynamics and impact behaviors. Clear differences in flow redirection, separation and overtopping dynamics, and consequential barrier responses among representative DF, DA, and RA cases can be observed from Movies S1, S2, and S3 (https://doi.org/10.25442/hku.20349192.v1; Kong & Guan, 2022).

3. Results and Discussion

3.1. Flow and Barrier Profiles Under Peak Impacts

Figure 3 displays key profiles under peak impact load F_b^{Peak} in Cases DF and RA with v_{int} = 6 m/s. Figures 3a and 3d indicate that F_b^{Peak} occurs during the overtopping process, where quasistatic dead zones (Faug, 2015; Kong, Zhao, et al., 2021) coexist with flowing layers. Thus, F_b^{Peak} should be calculated as the sum of loads from the dead zone and the flowing layer (see Figures A1e and A1f in Appendix A), especially in designing multilevel flexible barriers. Note that the boundaries of dead zones are roughly determined according to a velocity threshold (below 5% of incoming velocity; Faug et al., 2009). From another perspective, the dynamic load from flowing debris and the static load induced by both the dead zone and flowing layer can be transferred through contact networks to the barrier (Figures 3b and 3e). It reflects the rationality of hybrid analytical models (Faug, 2021; Wendeler et al., 2019) by considering hydrostatic and hydrodynamic components (Equation A4 in Appendix A). Indeed, the competitive roles of load components from the dead zone and flowing layer at different impact stages (i.e., frontal impact, runup impact, and overflow) drive the load sharing and distribution (Figures 4 and 6) and barrier load-deformation behavior (Figure 7).

Controlled by distinct flow materials, strong interparticle contacts occur outside-inside a triangle-shaped dead zone under the debris-flow impact (Figure 3b). In contrast, weak and more homogeneous contacts appear in a trapezoid-shaped dead zone under the impact of a rock avalanche (Figure 3e). It is mainly due to the dry flow undergoing a smaller bulk density and a higher energy dissipation efficiency of the flow-barrier interactions than the wet flow. Specifically, grain shear stress is considered more effective in energy dissipation than fluid viscous shearing (Fang et al., 2021; Song et al., 2018). The fluid phase can enhance flow mobility and thus impact pressures by dampening particle collisions (Kaitna et al., 2016) and decreasing interparticle friction (Iverson, 2003).

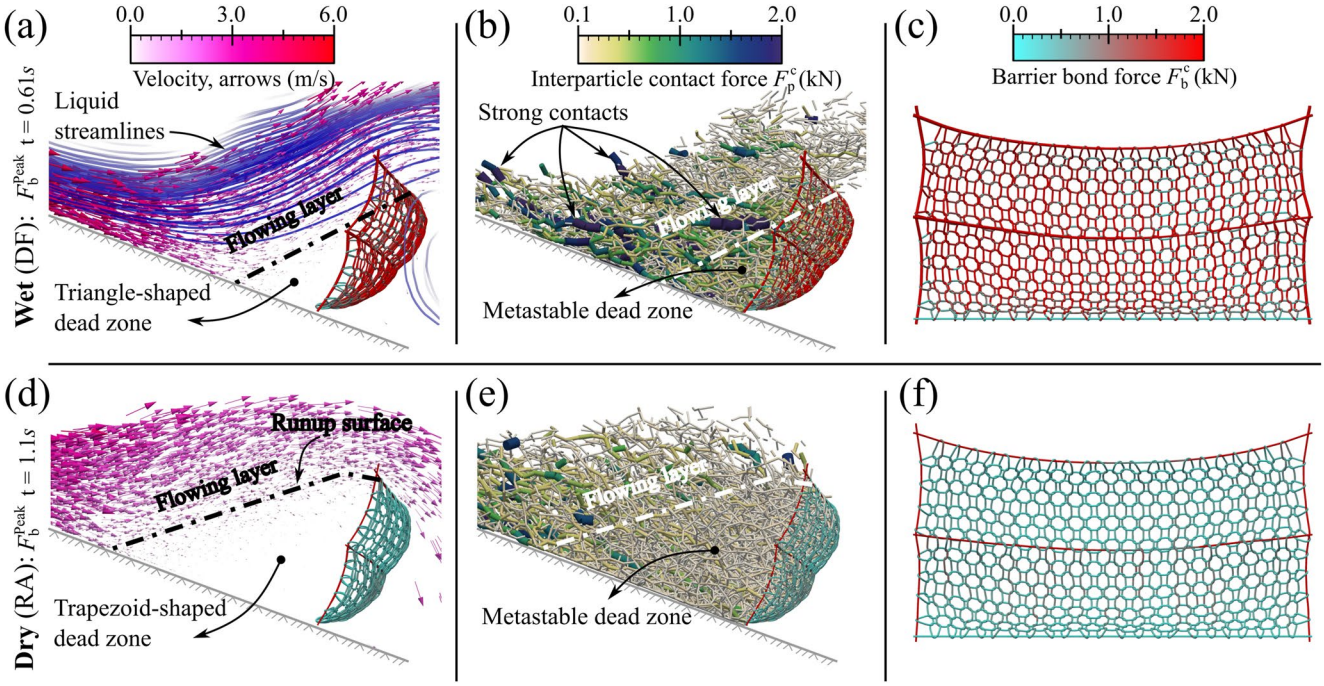

Figure 3. The flow velocities, interparticle contacts, and barrier load distributions at barrier peak impact F_b^{Peak} in arresting representative (a)–(c) wet and (d)–(f) dry flows.

They jointly explain why average barrier bond forces F_b^c in the wet case (Figure 3c) are more prominent than the dry case (Figure 3f), despite having similar pre-impact Fr numbers with the dry case. In this study, barrier bond forces are tensile forces sustained by parallel bonds that connect barrier nodal particles within different barrier components. Moreover, the maximum F_b^c is observed in cables, indicating effective load transfer from ring nets to cables. Interested readers can find details of impact dynamics under the largest barrier deformations (vertical and horizontal) and peak forces (cable and barrier) of the two representative cases in Figure B1 provided in Appendix B.

3.2. Flow-Barrier and In-Barrier Forces

3.2.1. Temporal Evolutions of Typical Flow-Barrier and In-Barrier Forces

The hybrid solid-fluid simulations enable the direct measures of the loads acting on either the flexible barrier system or an individual barrier component exerted by the solid and fluid phases in an impinging flow. In addition, the in-barrier forces, that is, the forces sustained within individual barrier components (i.e., the barrier bond force F_b^c) and the forces exerted by barrier components on each other, can also be extracted from the simulations. Taking the middle cable in a DF case as an example, Figure 4a demonstrates how the simulation captures the forces sustained by or acting on a cable. The left inset in Figure 4a illustrates that the bond force $F_b^{c,j}$ acting on a cable nodal particle j is contributed by flow impact (solid-cable contact force F_{s-c}^j and fluid-cable interaction force F_{f-c}^j), gravity F_g^j, and the portion through in-barrier load sharing (ring-cable contact force F_{r-c}^j).

Figure 4a compares the time-series data of four typical forces (F_{r-c}, T, F_{s-c}, and F_{f-c}) sustained by the middle cable in the DF case with $v_{int} = 6$ m/s. Specifically, the ring-cable contact force is calculated by $F_{r-c} = \sum_{j \in N_{MC}} F_{r-c}^j$, where N_{MC} denotes the total number of nodal particles in the middle cable. Analogously, the solid-cable contact and the fluid-cable interaction forces are calculated by $F_{s-c} = \sum_{j \in N_{MC}} F_{s-c}^j$ and $F_{f-c} = \sum_{j \in N_{MC}} F_{f-c}^j$, respectively. The cable tensile force is calculated by $T = \mathrm{Max}(F_b^{c,j})$, and the peak cable force $T^{Peak} = \mathrm{Max}(T)$ is extracted from the entire impact process. As shown in Figure 4a, similar trends between cable tensile force T and the ring-cable contact force F_{r-c} are observed, which differ significantly from F_{s-c} and F_{f-c}. Meanwhile, at T^{Peak}, T is around

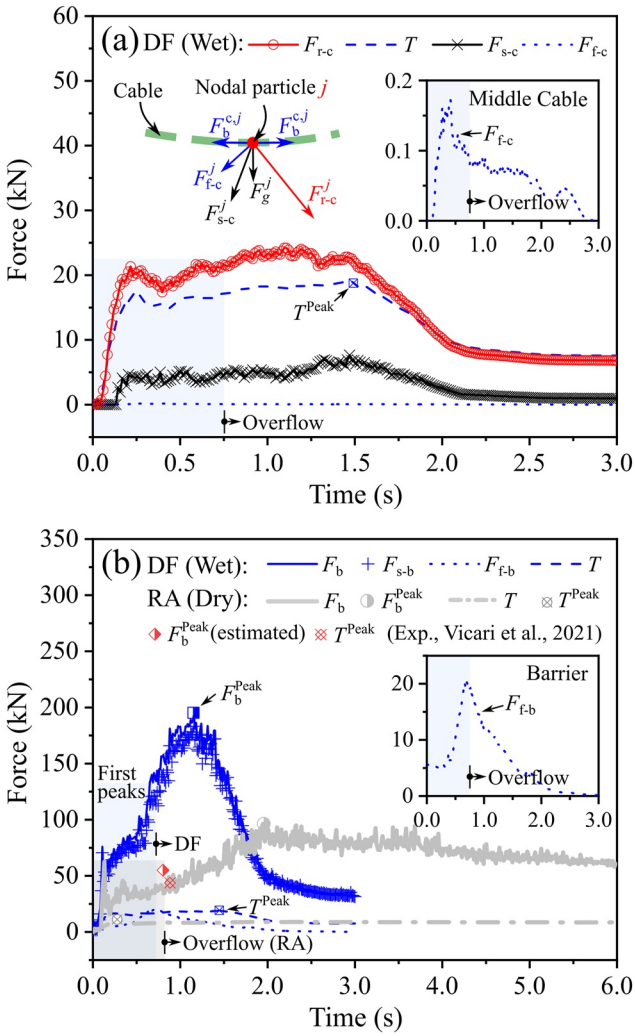

Figure 4. Temporal evolutions of (a) typical forces sustained by the middle cable from a wet case and (b) flow-barrier forces in representative wet and dry cases with v_{int} = 6 m/s.

three times larger than the sum of F_{s-c}, and F_{f-c}, while it is smaller than F_{r-c}. Therefore, the cable tensile force mainly results from the ring-cable force sharing rather than the direct debris-flow impact. The collective ring-cable contacts control cable forces, serving as a critical mechanism for effectively transferring flow impacts received by individual rings.

Figure 4b presents the temporal evolutions of flow-barrier forces, including the total impact load F_b, the solid-barrier contact force F_{s-b}, and the fluid-barrier interaction force F_{f-b}, in representative DF and RA cases. The cable tensile forces T sustained by the middle cable in the two cases are also plotted for comparison. The total impact load is calculated by $F_b = \sum_{i\in N_b} F_{s-b}^i + \sum_{i\in N_b} F_{f-b}^i$, where N_b represents the total number of barrier nodal particles. Thus, this model enables physics-informed measurement that delineates load components to F_b from individual debris-flow phases. Figure 4b reflects that the peak value F_{s-b} = 183.2 kN of the fluctuating solid-barrier contact force is around nine times larger than that (F_{f-b} = 20.3 kN, inset in Figure 4b) of the relatively smooth fluid-barrier interaction force. It indicates that the solid-barrier contact force is the dominant load contributor to the debris-flow impact. Compared with relatively smooth F_{f-b}, both random impacts caused by multiparticle force chains and random single-particle impacts control the fluctuations of F_{s-b} (see Figures B1c and B1d in Appendix B), similar to in-situ measures of basal force fluctuations in debris flows (Zhang et al., 2021). Under similar pre-impact Fr numbers, the first peaks caused by frontal impacts in the two cases are similar, while F_b^{Peak} = 96.3 kN occurring at overtopping in the dry case is about half of that (193.3 kN) in the wet case. Because rock avalanches undergo a higher energy dissipation efficiency and a smaller bulk density than debris flows, which hardly influence the first peak caused by the frontal impact but strongly affect the peak impact occurring at overflow. Although the absence of the fluid leads to a small bulk density of a dry case, the solid particles predominantly induce similar first peaks for the wet and dry cases.

Moreover, the valuable data of T^{Peak} and F_b^{Peak} from the experiment (Vicari et al., 2021) are plotted in Figure 4b for comparison under similar Fr conditions and barrier configurations (see details in Text S5 in Supporting Information S1). The experimental data T^{Peak} = 43.8 kN is around double T^{Peak} = 19.1 kN from our DF case since the experiment adopts a relatively high (1.5 m) and low-permeability (two layers) flexible ring net barrier. However, F_b^{Peak} = 55 kN estimated by the cable-based solution (Vicari et al., 2021) is around one in four of F_b^{Peak} = 193.3 measured from the DF case, indicating the cable-based solution may underestimate F_b^{Peak}. A further comparison of time-series cable tensile forces between this DF case and both large- and medium-scale flume tests (Vicari et al., 2021; Wang et al., 2022) can be found in Figure S5 in Supporting Information S1. The T^{Peak}-F_b^{Peak} relations from all numerical cases are presented in Figure 6 in Section 3.2.3.

3.2.2. Measured Relationships Underpinning Fr-Related Analytical Solutions

Figure 5a presents the influences of flow types and impact dynamics on the measured Fr-F_b^{Peak} relations, revealing bi-linear, positive correlations (average R^2 = 0.95). These identified bi-linear relationships are summarized in Table S1 in Supporting Information S1. Figures 5b–5d indicate that the inflection points of these identified bi-linear relationships are due to the shifts from trapezoid-to triangle-shaped dead zones measured at peak impacts (see details in Text S6 in Supporting Information S1). Here, the shifts (i.e., from slow to fast increases of F_b^{Peak} with Fr in Figure 5a; from trapezoid-to triangle-shaped dead zones in Figures 5b–5d) are further referred to identify the slow-to-fast transitions of flow impact dynamics for DFs, DAs, and RAs against a flexible barrier.

Figure 5a indicates that the increased solid fraction in an impinging flow results in the slow-to-fast transition occurring at a higher Fr, similar to impact mechanism transitions (e.g., from slow to fast, Faug, 2021; from

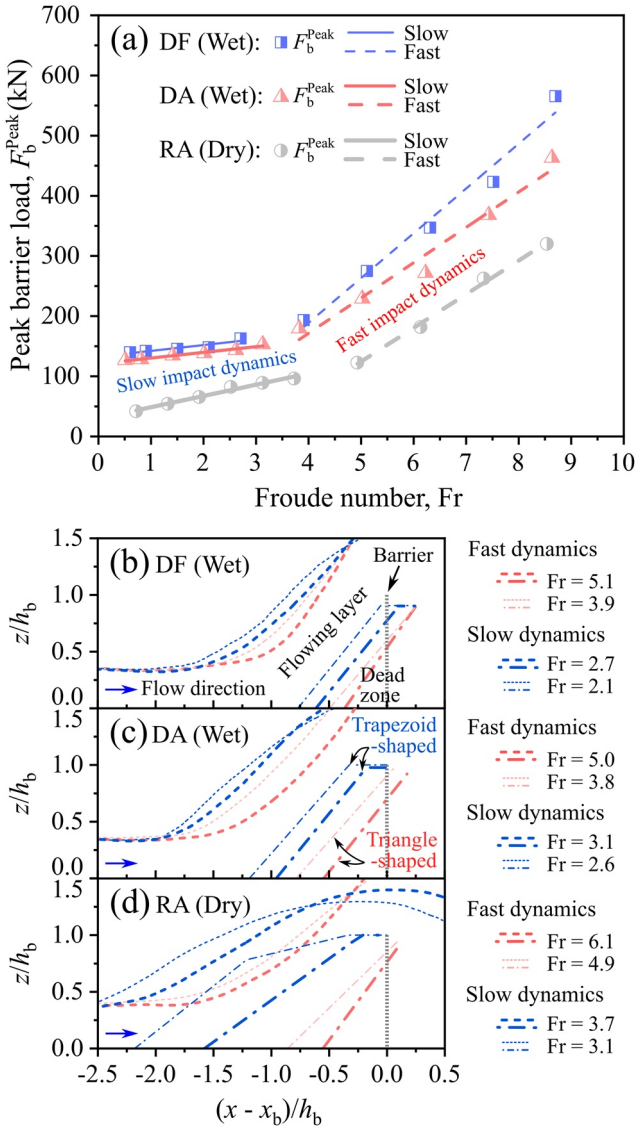

Figure 5. A unified diagram (a) showing how flow types and impact dynamics affect the measured Fr-F_b^{Peak} relations underpinning the Fr-related analytical solutions. (b)–(d) display free surfaces of flowing layers (dash lines) and boundaries of dead zones (dash-dotted lines) measured at peak impacts near the slow-to-fast transitions of impact dynamics in (a) for DF, DA, and RA cases, respectively. x_b and h_b denote the x-axis location and height of the barrier, respectively.

pile-up to runup, Kong, Li, et al., 2021; from momentum jump to vertical jet, Song et al., 2021). Furthermore, the increasing rates of Fr-F_b^{Peak} relations for DF (Fully saturated), DA (Partially saturated), and RA (Dry) cases under fast impact dynamics are much higher than that under slow impact dynamics (Figure 5a). Because impinging flows under slow impact dynamics experience a longer energy-dissipative runup surface (i.e., the boundary of a dead zone) and a larger volume of trapped debris at barrier peak impact than fast impact dynamics (Figures 5b–5d). Moreover, the increasing rate of Fr-F_b^{Peak} relations in DF cases under fast dynamics is 7.7 times that under slow dynamics, while the corresponding ratio is around 3 for RA cases. Our results highlight that the discriminants of impact dynamics (slow or fast) and flow types (DF, DA, or RA) are crucial for predicting Fr-F_b^{Peak} relations. These findings have fundamental implications for potential improvements of various Fr-related analytical solutions (details provided in Appendix A), which are commonly adopted for the practical design of flexible barriers in arresting different geophysical flows.

3.2.3. Correlations Between Peak Cable Force and Peak Barrier Load

Figure 6 displays the bi-linear, positive T^{Peak}-F_b^{Peak} relations (average $R^2 = 0.93$), with the inflection points and slopes altered by flow types and impact dynamics. These identified bi-linear relationships are summarized in Table S1 in Supporting Information S1. Under slow impact dynamics, the range of either T^{Peak} or F_b^{Peak} in the dry cases is much broader than the wet cases. Because the trapezoid-shaped dead zones in RA cases undergo more significant changes (i.e., runup surfaces and volume of trapped debris) than in DF and DA cases (see Figures 5b–5d). Moreover, the slopes of T^{Peak}-F_b^{Peak} relations for DF, DA, and RA cases are similar under either slow or fast impact dynamics. Their mean slope is around 13.7 under fast impact dynamics, approximately two times that (7.1) under slow impact dynamics. However, according to the cable-based solution (see Equation A6 in Appendix A), this slope should be much lower than 6 for a barrier configured with three horizontal cables. It indicates that the cable-based solution may underestimate the peak impact load of geophysical flows on a flexible barrier, especially under fast impact dynamics.

3.3. Barrier Load-Deformation Relationships

Quantifying barrier load-deformation relations is critical to evaluating the peak impact, barrier deformation, and retainment capacity for practical designs (EOTA, 2016; Kwan & Cheung, 2012). As shown in Figures 7a–7c, we categorize the barrier load-deformation behavior into the three dominant modes for DF (Fully saturated), DA (Partially saturated), and RA (Dry) cases with similar Fr numbers. D_h denotes the maximum barrier deflection in the flow direction (see Figure A1g in Appendix A). D_h and F_b are determined simultaneously from the entire flexible barrier system.

In mode *I* (Figure 7a), the equivalent barrier stiffness k_b^n undergoes two prominent stages: $k_{b,I}^n$ at the initial deformation stage and $k_{b,II}^n$ at the subsequent deformation stage. Note that the blue dotted auxiliary lines highlight the equivalent barrier stiffnesses $k_{b,I}^n$ and $k_{b,II}^n$ for the DF case. Initially, the barrier structure behaves flexibly with a small $k_{b,I}^n$ until the inflection point, at which point the majority of barrier flexibility is exhausted, and the equivalent barrier stiffness rapidly increases to $k_{b,II}^n$. In mode *II* (Figure 7b), F_b presents an increasing-decreasing-increasing trend before inflection points. The first peaks are primarily due to the direct impact of solid particles in a flow on the barrier during the frontal impact process (see Figures 4b, B1c, and B1d). Then, the formation of the dead zone impedes the direct impact of incoming solid particles on the barrier, which produces a short-term decrease of F_b. After that, the continuous increasing trend is possibly caused by the increasing static load induced

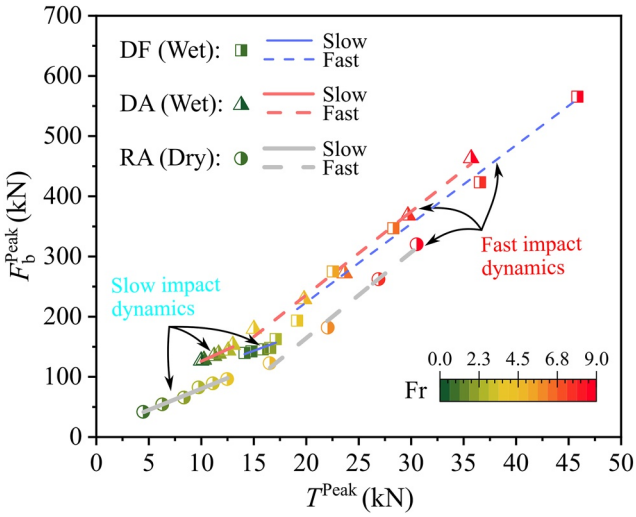

Figure 6. The influences of flow types and impact dynamics on the measured T^{Peak}-F_b^{Peak} relations. The slow-to-fast transitions of flow impact dynamics are consistent with Figure 5. Fr colors the symbols.

by the dead zone and the shear stress resulting from the flowing layer. Under modes *I* and *II*, overtopping occurs before the inflection points in dry (RA) cases while after the inflection points for wet (DF and DA) cases.

In mode *III* (Figure 7c), an interesting backward development trend of D_h along with a slight decrease of F_b near inflection points can be observed within a short duration before overtopping. This barrier shrinkage is due to the excessive barrier deformation resulting from the frontal impacts of flows carrying destructive momentum, which has been observed in the USGS flume tests (Logan et al., 2018). Under similar Fr number conditions (Figures 7b and 7c), the frontal impact-induced first peaks of F_b are roughly consistent between the wet and dry cases, while both F_b^{Peak} and Max(D_h) in the dry cases are smaller than the wet cases. Because the dry cases experience lower bulk density and higher energy dissipation efficiency than the wet cases, which slightly affects the first peak induced by the frontal impact but strongly influences the peak impact and maximum barrier deformation occurring at overflow.

Figure 7d further compiles a flow-specific diagram to clarify the three Fr-dependent modes of barrier load-deformation behaviors and their key determining parameters and typical physical impacting processes. The legend/table in Figure 7d only presents the measured upper or lower limits of the flow-specific Fr conditions for each mode in this study. The recognition of the barrier load-deformation mode for an impinging flow with a Froude number in between different modes needs further investigation. Details of the flow-specific Fr conditions for the transitions of predominant barrier load-deformation modes are presented in Figure S7 in Supporting Information S1. The shaded areas below F_b-D_h lines indicate strain energy stored by the barrier to a certain extent. Assuming a piecewise linear increase of the load F_b, plotted over the deformation D_h, produces barrier strain energy at F_b^{Peak}. Consequently, the examination of F_b-D_h relations may help quantify barrier strain energy and understand the complicated energy dissipation process. Moreover, higher Fr produces larger shaded areas before F_b^{Peak} (Figure 7d), and the wet cases present larger areas below the barrier load-deformation curves than the dry case despite having similar pre-impact Fr numbers with the dry case (Figure 7b). It indicates that barrier structural deformability can be utilized to the best advantage in dissipating impact energy when subjected to high-velocity wet flows. Note that large boulders commonly observed in natural geophysical flows (Belli et al., 2022; Iverson et al., 2011) can produce much higher peak impact loads and significantly change the barrier load-deformation behavior. Thus, the three generalized modes only apply to geophysical flows with distributed and continuous loading characteristics.

Figure 7e presents the Max(D_h)-F_b^{Peak} relations underpinning the spring solution (see Figure A1g in Appendix A), displaying the bi-linear, positive correlations with an average $R^2 = 0.93$. These bi-linear relationships are summarized in Table S1 in Supporting Information S1. Both Max(D_h) and F_b^{Peak} are crucial designing factors and positively correlated with Fr. For either wet (DF and DA) or dry (RA) flows, fast impact dynamics witness a higher increasing rate of F_b^{Peak} with Max(D_h) than slow impact dynamics. Because the trapezoid-shaped dead zones under slow impact dynamics experience the longer energy-dissipative runup surface and the larger volume of trapped debris than the triangle-shaped ones under fast impact dynamics (see Figures 5b–5d). Further, the slopes of the bi-linear Max(D_h)-F_b^{Peak} relation in dry cases under slow and fast impact dynamics are around half that in wet cases, owing to the energy dissipation efficiencies of the flowing layer and dead zone in wet flows being lower than in dry flows. Similar trends of the bi-linear Max(D_h)-F_b^{Peak} relations are observed in DF and DA cases, while the magnitudes of Max(D_h) and F_b^{Peak} in DA cases are much smaller than in DF cases under similar pre-impact Fr numbers. Our results indicate that flow materials (either wet or dry flows) primarily control the trend of Max(D_h)-F_b^{Peak} relations, while a larger bulk density in a wet flow produces more significant Max(D_h) and F_b^{Peak} under similar pre-impact Fr numbers.

The inset in Figure 7e reveals the bi-linear, positive correlations between Fr and k_b^n with an average R^2 of 0.92. The equivalent barrier stiffness, that is, $k_b^n = F_b^{Peak}/\text{Max}(D_h)$, is determined from the complete impact process for each case. Under slow impact dynamics, k_b^n is roughly constant in either dry (RA: ~ 0.26 MN/m) or wet cases

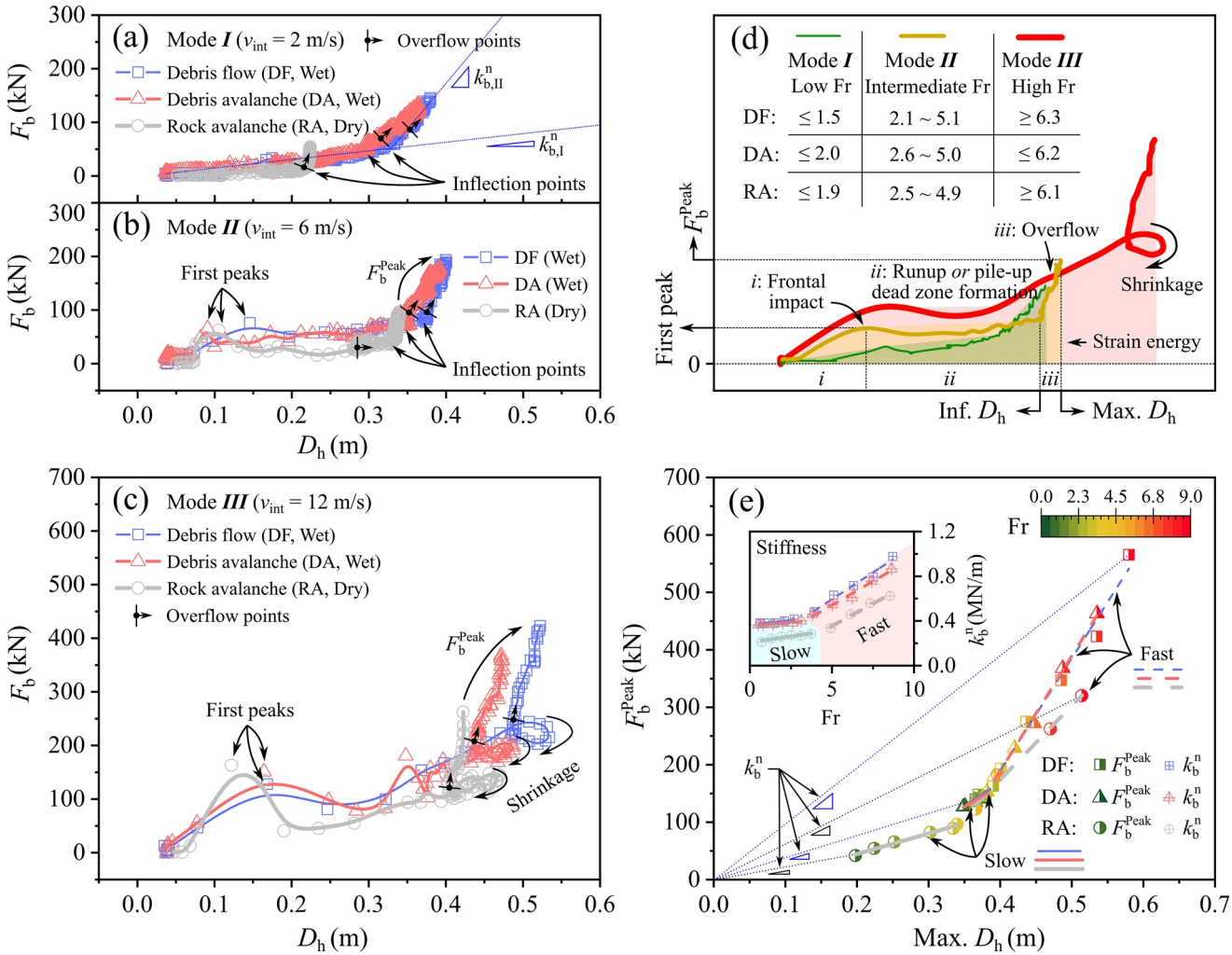

Figure 7. Three Fr-dependent modes (a)–(d) for barrier load-deformation (F_b-D_h) behaviors in arresting debris flows, debris avalanches, and rock avalanches. A unified diagram (e) presents the influences of flow materials and impact dynamics on Max(D_h)-F_b^{Peak} and Fr-k_b^n relations. The transitions of flow impact dynamics from slow to fast in (e) are consistent with Figures 5 and 6.

(DF: ~ 0.39 MN/m; DA: ~ 0.38 MN/m). Under fast impact dynamics, k_b^n increases rapidly with increasing Fr in DF, DA, and RA cases, wherein RA (dry) cases experience the minimum growth rate. It indicates that k_b^n changes with flow materials and Fr conditions under fast impact dynamics, regardless of the same barrier. Therefore, the hypothesis of constant k_b^n in spring solution can be reasonable under slow impact dynamics, whereas its rationality is not guaranteed under fast impact dynamics or with different impinging flows.

4. Conclusions

This study presents systematic, high-fidelity simulations of a flexible barrier system against debris flows, debris avalanches, and rock avalanches, corresponding to distinct flow dynamics and impact behaviors. The employed continuum-discrete coupling model captures the essential physics observed in experiments and field investigations. The results support the following conclusions:

1. This study enables physics-informed numerical measures of the total impact loads of debris flows/avalanches and rock avalanches on a flexible ring net barrier system, delineating the contributions of individual phases to the total impact. The results highlight that the fluctuating solid-barrier contact force and the overflow process are the predominant load contributor and the critical impact stage for determining peak impact loads of geophysical flows on flexible barriers, respectively.

2. For the first time, a systematic examination of the flow-barrier forces, in-barrier forces, and barrier load-deformation relations reveals the unified bi-linear laws, which underpin widely used analytical and simplified solutions. Our results indicate that the spring and cable-based solutions may introduce errors in estimating the peak impact loads exerted on flexible barriers by geophysical flows, especially under fast impact dynamics. We also compile a flow-specific diagram to clarify three Froude-number-dependent modes of barrier load-deformation behaviors.
3. The identified bi-linear relationships quantitatively link the peak barrier load to impinging flow properties scaled by the Froude number, the peak cable force, or the maximum barrier deformation. Their flow-specific inflection points are caused by the transitions from trapezoid-shaped to triangle-shaped dead zones measured at peak impacts. These findings facilitate predicting the impact load of geophysical flows on flexible barriers based on flow materials (wet vs. dry) and impact dynamics (slow vs. fast).

This study helps to advance our understanding of the physical laws of multiphase, multiway flow-barrier interactions. The findings in this paper offer a physics-based, crucial improvement over existing solutions to impact problems for geophysical flows.

Appendix A: Analytical and Simplified Solutions in Estimating Peak Impact Load

This appendix revisits key assumptions and equations of analytical and simplified solutions for estimating impact loads of geophysical flows on flexible barriers. According to the three key impact stages shown in Figures A1a–A1f illustrate the impact loading history with the dynamic load F_b^{dyn} from flowing debris, the static load F_b^{sta} induced by dead zone and flowing layer, as well as the passive pressure F_b^{pas} and the drag or shear force F_b^{dra} produced by the overtopping or flowing layer. As a result, the total impact load F_b can be cast as:

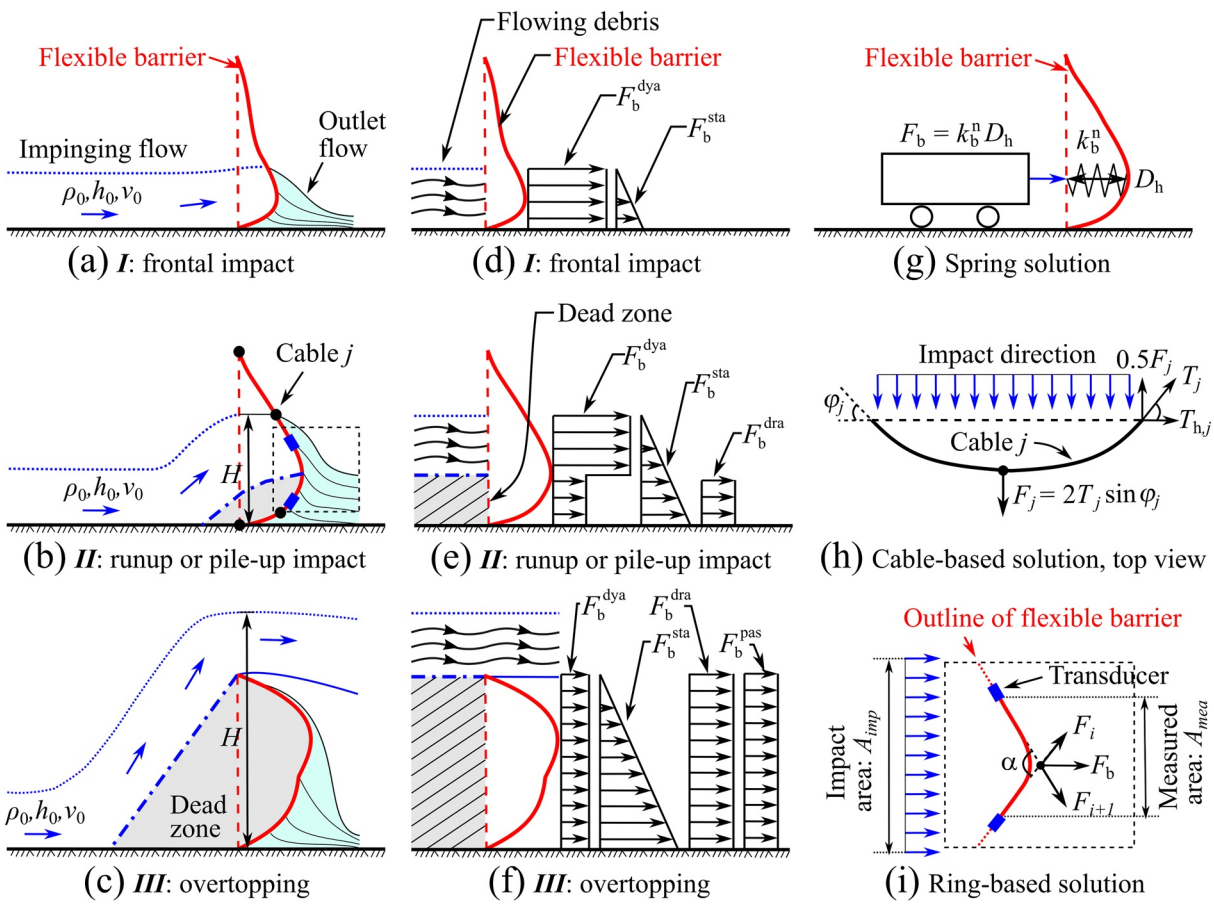

Figure A1. Sketches of (a)–(c) the conceptualizations for analytical solutions and (d)–(f) the impact load components at three key flow-barrier interactions between geophysical flows and a flexible barrier. (g)–(i) illustrates three simplified solutions based on the typical impact process in (b).

$$F_b = F_b^{dyn} + F_b^{sta} + F_b^{pas} + F_b^{dra} \tag{A1}$$

where the direct-impact induced force dominates at the frontal impact (Figures A1d), while forces produced by the dead zone and flowing layer play substantial roles during overflow (Ashwood & Hungr, 2016; Figures A1f). Although these load components are crucial for evaluating impact loads on flow-resisting rigid and flexible barriers (Jiang et al., 2021; Tan et al., 2020; Vagnon & Segalini, 2016), quantitative determination of their values remains a long-standing question.

A1. Analytical Solutions

In simplest terms, Fr-related analytical solutions, including hydrodynamic, hydrostatic, and hybrid models, have been developed for designing flexible barriers. Notably, Fr is universally used to characterize flow dynamics and aid barrier designs (Kyburz et al., 2020; Wendeler, 2016). It is defined as $\mathrm{Fr} = v_0/\sqrt{g h_0 \cos\theta}$, where v_0 and h_0 represent flow velocity and depth. Based on the frontal impact process (Figure A1a), the hydrodynamic formula (Hungr et al., 1984) is expressed as:

$$F_b = \alpha \rho_0 v_0^2 h_0 w \tag{A2}$$

where α is the hydrodynamic coefficient, ρ_0 is flow bulk density, and w is the width of the barrier. α assumes a purely fluid-like force proportional to the velocity square in the inertial regime at high Fr. In comparison, the hydrostatic formula (Armanini, 1997) is given by:

$$F_b = \kappa \rho_0 g h_0^2 w \tag{A3}$$

where κ represents the empirical hydrostatic coefficient, assuming a hydrostatic force contribution in the gravity regime at low Fr (Faug, 2021).

For the subsequent impact processes (Figures A1b and A1c), the hybrid models are proposed considering hydrostatic and hydrodynamic factors (e.g., Faug, 2021; Li, Zhao, & Soga, 2021; Song et al., 2022). For instance, the hybrid formula (Wang et al., 2022; Wendeler et al., 2019) can be expressed as:

$$F_b = \alpha \rho_0 v_0^2 h_0 w + \kappa \rho_0 g H^2 w \tag{A4}$$

where H is the total height of the static deposit and flowing layer. In practice, these empirical coefficients (α and κ) and functions are in conjunction with Fr that have been widely adopted in designing flexible, slit, and rigid barriers (Kong et al., 2022; Li, Zhao, & Soga, 2021).

A2. Simplified Solutions

Based on the impact process shown in Figure A1b and A1g–A1i illustrate alternative simplified solutions that rely on barrier deformations, cable forces, and ring-ring contact forces. These solutions have been adopted in experimental and in-suit tests to estimate the impacts of geophysical flows on flexible barriers (Ashwood & Hungr, 2016; Lam et al., 2022; Ng et al., 2017; Song et al., 2022; Tan et al., 2019; Wendeler, 2016). For instance, the spring solution (Figure A1g) is expressed as:

$$F_b = k_b^n D_h \tag{A5}$$

where k_b^n and D_h denote the equivalent barrier stiffness and maximum barrier deflection in the flow direction. This solution assumes a constant k_b^n of a flexible barrier.

Figure A1h illustrates the simplified force analysis based on the top view of the horizontal supporting cable j in Figure A1b. This cable-based simplified solution converts cable tensile force T_j to the impact load normal to the barrier face F_j (Ferrero et al., 2015; Ng et al., 2017). The sum of F_j measured in each cable is assumed to be the

total impact load F_b. It estimates F_b based on the horizontal deflection angle of cable j (φ_j) and T_j, according to the following equation:

$$F_b = \sum_{j=1}^{n} 2T_j \sin \varphi_j \tag{A6}$$

where n is the number of horizontal cables, typically ranging from 2 to 4 in experiments (Ng et al., 2017; Vicari et al., 2021).

Figure A1i displays the simplified force analysis of the measured area (dash box in Figure A1b) in the cross-section of transducer i and transducer $i+1$. The transducers in-between connected rings have been used to record their maximum tensile force, for example, F_i in the transducer i. This ring-based simplified solution (Tan et al., 2018) calculates F_b by:

$$F_b = \cos\frac{\alpha}{2}\left(\sum_{i=1}^{n} F_i\right)\frac{A_{imp}}{A_{mea}} \tag{A7}$$

where F_i is the ring-ring contact force, α is the included angle of deformed cross-sectional barrier, and $\frac{A_{imp}}{A_{mea}}$ denotes the load area ratio. We did not examine this ring-based simplified solution due to the difficulties in modeling the specific laboratory equipment used by Tan et al. (2018, 2019).

These analytical and simplified solutions feature simple expressions with idealized assumptions and easy-to-estimate inputs. For instance, barrier and cable deformations are 3D phenomena, varying across the width and height of the barrier, and the length of a cable, which differs significantly from these simplified solutions. Thus, there is a pressing need to assess their validity by virtue of physics-based direct measures of the inter-twined relations among barrier load, impinging flow properties, cable force, and barrier deformation.

Appendix B: Dynamics at Largest Deformations and Peak Forces

Figure B1 presents the impact dynamics and barrier load distributions at the largest deformations (maximum D_v and maximum D_h) and peak forces (peak barrier load F_b^{Peak} and peak cable force T^{Peak}) of a flexible barrier in arresting representative wet (DF) and dry (RA) flows. D_v and D_h denote the maximum deformations perpendicular to and along the flow direction, respectively. The fluid part in the DF case (Figure B1a) is visualized by the contour surface of the liquid phase with liquid fraction $\alpha_l = 0.5$ and in the background color with transparency equal to 50%. The magnitudes of interparticle contact force F_p^c and barrier bond force F_b^c are denoted by the thickness and color of tubes. The *I*, *II,* and *III* denote three key flow-barrier interactions, including frontal impact, runup impact, and overtopping processes (Kong, Li, et al., 2021).

Figure B1 indicates F_b^{Peak}, T^{Peak}, and maximum D_v and maximum D_h do not occur simultaneously. Thus, it may lack rationality that a simplified solution empirically links the peak cable force or the maximum barrier deformations to F_b^{Peak}. Furthermore, the maximum D_v occurs at stage *II* (runup process) for both wet and dry cases (Figures B1a-2 and B1b-2) because the barrier will reduce in height immediately when subjected to the frontal impact of impinging flows. This vertical deformation influences barrier containment capacity and therefore affects both the load acting on the barrier and the final barrier deformation.

Figures B1c and B1d show the side views of solid-barrier interactions visualized in contact fabric networks for the wet and dry cases, respectively. Strong contact forces are denoted in black and are relatively thicker than weak contact forces in gray. At stage *I* (Figures B1c-1 and B1d-1), strong force chains are observed at the bottom of barriers for both cases. Then, some solid particles can directly impact the middle part of the barrier at stage *II* (Figures B1c,2, B1d,1 and B1d-2). It may partially explain why T^{Peak} can occur at stage *II* for a dry case (Figure B1d-3). During impact stage *III*, strong contacts mainly happen at the lower and higher parts of dead zones in the wet case, while no strong contact has been observed in the dry case (Figures B1d-4 and B1d-5) Compared with the wet case, the metastable dead zone forms faster in the dry case, wherein the interparticle contact forces restrict retained particles from moving, resulting in an effective energy-dissipating contact network.

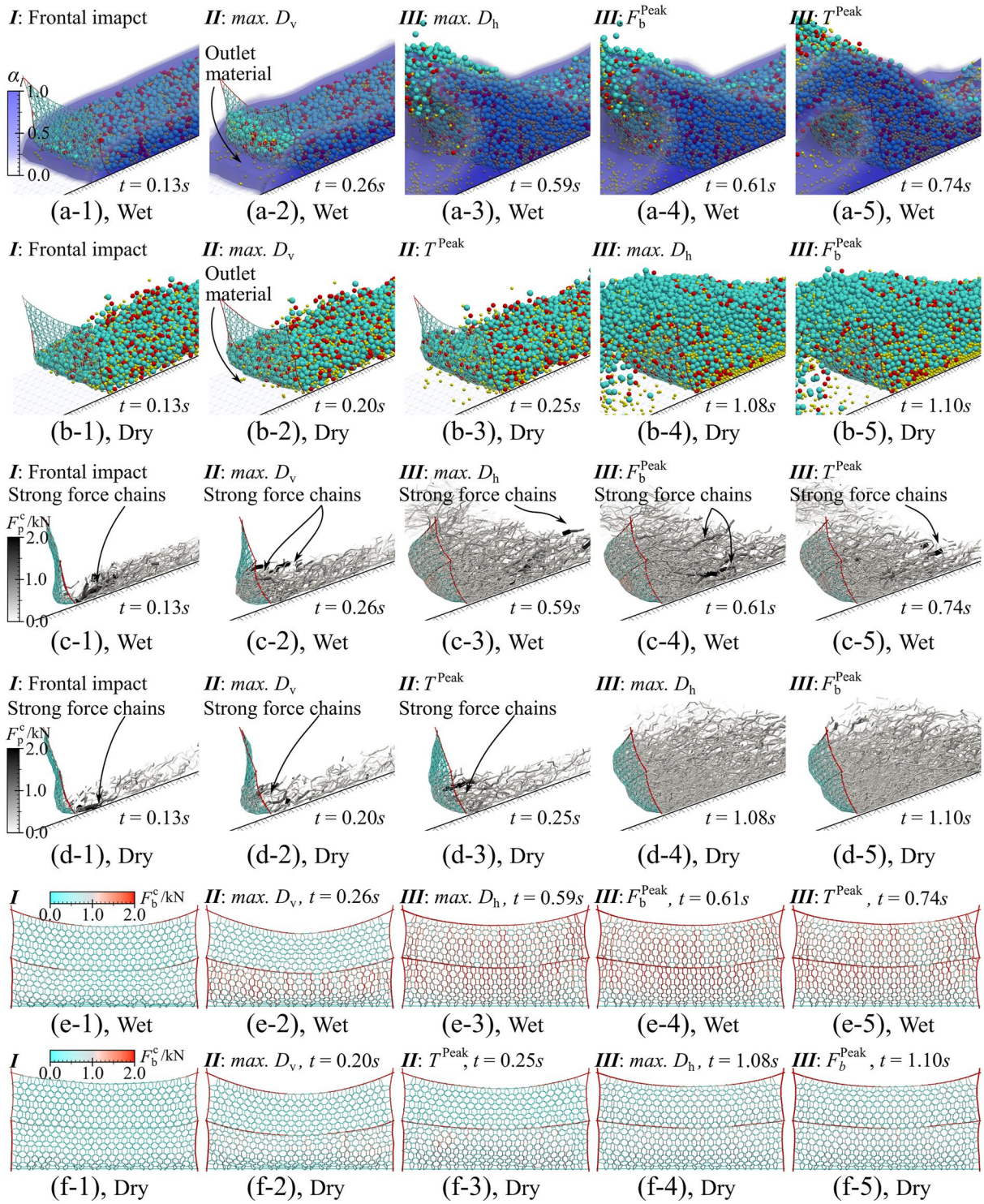

Figure B1. Comparisons of impact dynamics and barrier load distributions at largest deformations (maximum D_v and maximum D_h) and peak forces (F_b^{Peak} and T^{Peak}) of a flexible ring net barrier in arresting debris flow (a)–(e) and rock avalanche (b)–(f) with v_{int} = 6 m/s.

Figures B1e and B1f display the barrier load distributions for the two cases. For both cases, the lower half part of the ring net is observed with concentrated loads at stage *II*, and the load distributions are relatively homogeneous throughout the entire ring net at stage *III*. The observed changes in load concentration are caused by the dynamic load transfer mechanisms within the barrier and the sharing of static loads for the trapped solid mass in a dead

zone during stages *II* and *III*. The gradual change of shear forces induced by the flowing layer at stages *II* and *III* also contributes to this phenomenon (see Figures A1e and A1f in Appendix A). Moreover, the vertical stretching is more significant than the horizontal stretching of the ring net during stage *III* (Figures B1e and B1f). It is due to the downward momentum transfer from incoming flows, the continuously increased static load induced by the dead zone, as well as more shear stress and earth pressure from the flowing layer transferred through the metastable contact networks to the barrier (see Figure A1f in Appendix A). Therefore, the competitive roles of macroscopic load components from the flowing debris and the dead zone at different impact stages drive the characteristics of flow-barrier force transmissions and barrier load distributions.

Conflict of Interest

The authors declare no conflicts of interest relevant to this study.

Data Availability Statement

The supplementary videos (Figure 1) and data set (Figures 4–7, and Figure S7 in Supporting Information S1) underlying this article are permanently archived at https://doi.org/10.25442/hku.20349192.v1 (Kong & Guan, 2022). The code used to produce the coupled CFD-DEM simulations is licensed under GNU and published on GitHub https://github.com/CFDEMproject/CFDEMcoupling-PUBLIC/ (CFDEMproject, 2017).

Acknowledgments
The research reported in this work is financially supported by the National Natural Science Foundation of China (Project #51909227 and #11972030) and the University Grants Council of Hong Kong (RGC/GRF Project #27202419 and #16205418).

References

Albaba, A., Lambert, S., Kneib, F., Chareyre, B., & Nicot, F. (2017). DEM modeling of a flexible barrier impacted by a dry granular flow. *Rock Mechanics and Rock Engineering*, *50*(11), 3029–3048. https://doi.org/10.1007/s00603-017-1286-z

Armanini, A. (1997). On the dynamic impact of debris flows. In A. Armanini, & M. Michiue (Eds.), *Recent developments on debris flows* (pp. 208–226). Springer.

Ashwood, W., & Hungr, O. (2016). Estimating total resisting force in flexible barrier impacted by a granular avalanche using physical and numerical modeling. *Canadian Geotechnical Journal*, *53*(10), 1700–1717. https://doi.org/10.1139/cgj-2015-0481

Belli, G., Walter, F., McArdell, B., Gheri, D., & Marchetti, E. (2022). Infrasonic and seismic analysis of debris-flow events at Illgraben (Switzerland): Relating signal features to flow parameters and to the seismo-acoustic source mechanism. *Journal of Geophysical Research: Earth Surface*, *127*(6), e2021JF006576. https://doi.org/10.1029/2021JF006576

Berger, C., Denk, M., Graf, C., Stieglitz, L., & Wendeler, C. (2021). Practical guide for debris flow and hillslope debris flow protection nets. *WSL Berichte*, *113*, 79.

Berger, C., McArdell, B. W., & Schlunegger, F. (2011). Direct measurement of channel erosion by debris flows, Illgraben, Switzerland. *Journal of Geophysical Research*, *116*(F1), F01002. https://doi.org/10.1029/2010JF001722

Breard, E. C., Dufek, J., Fullard, L., & Carrara, A. (2020). The basal friction coefficient of granular flows with and without excess pore pressure: Implications for pyroclastic density currents, water-rich debris flows, and rock and submarine avalanches. *Journal of Geophysical Research: Solid Earth*, *125*(12), e2020JB020203. https://doi.org/10.1029/2020JB020203

Brighenti, R., Segalini, A., & Ferrero, A. M. (2013). Debris flow hazard mitigation: A simplified analytical model for the design of flexible barriers. *Computers and Geotechnics*, *54*, 1–15. https://doi.org/10.1016/j.compgeo.2013.05.010

Bugnion, L., McArdell, B. W., Bartelt, P., & Wendeler, C. (2012). Measurements of hillslope debris flow impact pressure on obstacles. *Landslides*, *9*(2), 179–187. https://doi.org/10.1007/s10346-011-0294-4

Cabrera, M., & Estrada, N. (2021). Is the grain size distribution a key parameter for explaining the long runout of granular avalanches? *Journal of Geophysical Research: Solid Earth*, *126*(9), e2021JB022589. https://doi.org/10.1029/2021JB022589

Caviezel, A., Ringenbach, A., Demmel, S. E., Dinneen, C. E., Krebs, N., Bühler, Y., et al. (2021). The relevance of rock shape over mass—Implications for rockfall hazard assessments. *Nature Communications*, *12*(1), 5546. https://doi.org/10.1038/s41467-021-25794-y

CFDEMproject. (2017). CFDEMcoupling-PUBLIC. [Software]. Github. Retrieved from https://github.com/CFDEMproject/CFDEMcoupling-PUBLIC.git

Cook, K. L., Rekapalli, R., Dietze, M., Pilz, M., Cesca, S., Rao, N. P., et al. (2021). Detection and potential early warning of catastrophic flow events with regional seismic networks. *Science*, *374*(6563), 87–92. https://doi.org/10.1126/science.abj1227

Coussot, P., Laigle, D., Arattano, M., Deganutti, A., & Marchi, L. (1998). Direct determination of rheological characteristics of debris flow. *Journal of Hydraulic Engineering*, *124*(8), 865–868. https://doi.org/10.1061/(ASCE)0733-9429(1998)124:8(865)

Cui, P., Zeng, C., & Lei, Y. (2015). Experimental analysis on the impact force of viscous debris flow. *Earth Surface Processes and Landforms*, *40*(12), 1644–1655. https://doi.org/10.1002/esp.3744

De Haas, T., Åberg, A. S., Walter, F., & Zhang, Z. (2021). Deciphering seismic and normal-force fluctuation signatures of debris flows: An experimental assessment of effects of flow composition and dynamics. *Earth Surface Processes and Landforms*, *46*(11), 2195–2210. https://doi.org/10.1002/esp.5168

De Natale, J. S., Iverson, R. M., Major, J. J., LaHusen, R. G., Fiegel, G. L., & Duffy, J. D. (1999). *Experimental testing of flexible barriers for containment of debris flows*. US Department of the Interior, US Geological Survey. https://doi.org/10.3133/OFR99205

Dugelas, L., Coulibaly, J. B., Bourrier, F., Lambert, S., Chanut, M. A., Olmedo, I., & Nicot, F. (2019). Assessment of the predictive capabilities of discrete element models for flexible rockfall barriers. *International Journal of Impact Engineering*, *133*, 103365. https://doi.org/10.1016/j.ijimpeng.2019.103365

EOTA. (2016). Flexible kits for retaining debris flows and shallow landslides/open hill debris flows. EAD 340020-00-0106. Retrieved from https://www.nlfnorm.cz/en/ehn/6329

Fang, J., Wang, L., Hong, Y., & Zhao, J. (2021). Influence of solid-fluid interaction on impact dynamics against rigid barrier: CFD-DEM modelling. *Géotechnique*, *72*(5), 391–406. https://doi.org/10.1680/jgeot.19.P.160

Faug, T. (2015). Depth-averaged analytic solutions for free-surface granular flows impacting rigid walls down inclines. *Physical Review E*, *92*(6), 062310. https://doi.org/10.1103/PhysRevE.92.062310

Faug, T. (2021). Impact force of granular flows on walls normal to the bottom: Slow versus fast impact dynamics. *Canadian Geotechnical Journal*, *58*(1), 114–124. https://doi.org/10.1139/cgj-2019-0399

Faug, T., Beguin, R., & Chanut, B. (2009). Mean steady granular force on a wall overflowed by free-surface gravity-driven dense flows. *Physical Review E*, *80*(2), 021305. https://doi.org/10.1103/PhysRevE.80.021305

Faug, T., Caccamo, P., & Chanut, B. (2012). A scaling law for impact force of a granular avalanche flowing past a wall. *Geophysical Research Letters*, *39*(23), L23401. https://doi.org/10.1029/2012GL054112

Fávero Neto, A. H., Askarinejad, A., Springman, S. M., & Borja, R. I. (2020). Simulation of debris flow on an instrumented test slope using an updated Lagrangian continuum particle method. *Acta Geotechnica*, *15*(10), 2757–2777. https://doi.org/10.1007/s11440-020-00957-1

Ferrero, A. M., Segalini, A., & Umili, G. (2015). Experimental tests for the application of an analytical model for flexible debris flow barrier design. *Engineering Geology*, *185*, 33–42. https://doi.org/10.1016/j.enggeo.2014.12.002

GEOVERT. (2016). GeoHazard mitigation: Shenandoah debris flow barrier. Retrieved from https://www.geovert.com/gedp-past-projects/Shenandoah/Debris-Flow-Barrier

Goniva, C., Kloss, C., Deen, N. G., Kuipers, J. A., & Pirker, S. (2012). Influence of rolling friction on single spout fluidized bed simulation. *Particuology*, *10*(5), 582–591. https://doi.org/10.1016/j.partic.2012.05.002

Hoch, O. J., McGuire, L. A., Youberg, A. M., & Rengers, F. K. (2021). Hydrogeomorphic recovery and temporal changes in rainfall thresholds for debris flows following wildfire. *Journal of Geophysical Research: Earth Surface*, *126*(12), e2021JF006374. https://doi.org/10.1029/2021JF006374

Hungr, O., Morgan, G. C., & Kellerhals, R. (1984). Quantitative analysis of debris torrent hazards for design of remedial measures. *Canadian Geotechnical Journal*, *21*(4), 663–677. https://doi.org/10.1139/t84-073

Iverson, R. M. (1997). The physics of debris flows. *Reviews of Geophysics*, *35*(3), 245–296. https://doi.org/10.1029/97RG00426

Iverson, R. M. (2003). The debris-flow rheology myth. Debris-flow hazards mitigation: Mechanics, prediction, and assessment. *1*, 303–314.

Iverson, R. M., George, D. L., & Logan, M. (2016). Debris flow runup on vertical barriers and adverse slopes. *Journal of Geophysical Research: Earth Surface*, *121*(12), 2333–2357. https://doi.org/10.1002/2016JF003933

Iverson, R. M., Reid, M. E., Logan, M., LaHusen, R. G., Godt, J. W., & Griswold, J. P. (2011). Positive feedback and momentum growth during debris-flow entrainment of wet bed sediment. *Nature Geoscience*, *4*(2), 116–121. https://doi.org/10.1038/ngeo1040

Jiang, Y. J., Fan, X. Y., Su, L. J., Xiao, S. Y., Sui, J., Zhang, R. X., et al. (2021). Experimental validation of a new semi-empirical impact force model of the dry granular flow impact against a rigid barrier. *Landslides*, *18*(4), 1387–1402. https://doi.org/10.1007/s10346-020-01555-8

Kaitna, R., Palucis, M. C., Yohannes, B., Hill, K. M., & Dietrich, W. E. (2016). Effects of coarse grain size distribution and fine particle content on pore fluid pressure and shear behavior in experimental debris flows. *Journal of Geophysical Research: Earth Surface*, *121*(2), 415–441. https://doi.org/10.1002/2015JF003725

Kong, Y., & Guan, M. F. (2022). Dataset and supplementary movies for geophysical mass flows against a flexible ring net barrier. [Dataset]. HKU Data Repository. https://doi.org/10.25442/hku.20349192.v1

Kong, Y., Guan, M. F., Li, X. Y., Zhao, J. D., & Yan, H. C. (2022). How flexible, slit and rigid barriers mitigate two-phase geophysical mass flows: A numerical appraisal. *Journal of Geophysical Research: Earth Surface*, *127*(6), e2021JF006587. https://doi.org/10.1029/2021JF006587

Kong, Y., Li, X., & Zhao, J. (2021). Quantifying the transition of impact mechanisms of geophysical flows against flexible barrier. *Engineering Geology*, *289*, 106188. https://doi.org/10.1016/j.enggeo.2021.106188

Kong, Y., Zhao, J., & Li, X. (2021). Hydrodynamic dead zone in multiphase geophysical flows impacting a rigid obstacle. *Powder Technology*, *386*, 335–349. https://doi.org/10.1016/j.powtec.2021.03.053

Kwan, J. S. H., & Cheung, R. W. M. (2012). *Suggestion on design approaches for flexible debris-resisting barriers. Discussion Note DN1/2012*. The Government of Hong Kong Standards and Testing Division.

Kyburz, M. L., Sovilla, B., Gaume, J., & Ancey, C. (2020). Decoupling the role of inertia, friction, and cohesion in dense granular avalanche pressure build-up on obstacles. *Journal of Geophysical Research: Earth Surface*, *125*(2), e2019JF005192. https://doi.org/10.1029/2019JF005192

Lam, H. W., Sze, E. H. Y., Wong, E. K. L., Poudyal, S., Ng, C. W. W., Chan, S. L., & Choi, C. E. (2022). Study of dynamic debris impact load on flexible debris-resisting barriers and the dynamic pressure coefficient. *Canadian Geotechnical Journal*. e-First. https://doi.org/10.1139/cgj-2021-0325

Leonardi, A., Cabrera, M., Wittel, F. K., Kaitna, R., Mendoza, M., Wu, W., & Herrmann, H. J. (2015). Granular-front formation in free-surface flow of concentrated suspensions. *Physical Review E*, *92*(5), 052204. https://doi.org/10.1103/PhysRevE.92.052204

Leonardi, A., Wittel, F. K., Mendoza, M., Vetter, R., & Herrmann, H. J. (2016). Particle-fluid-structure interaction for debris flow impact on flexible barriers. *Computer-Aided Civil and Infrastructure Engineering*, *31*(5), 323–333. https://doi.org/10.1111/mice.12165

Li, B., Wang, C., Li, Y., & Zhang, S. (2021). Dynamic response study of impulsive force of debris flow evaluation and flexible retaining structure based on SPH-DEM-FEM coupling. *Advances in Civil Engineering*, *2021*(12), 9098250. https://doi.org/10.1155/2021/9098250

Li, D., Lu, X., Walling, D. E., Zhang, T., Steiner, J. F., Wasson, R. J., et al. (2022). High Mountain Asia hydropower systems threatened by climate-driven landscape instability. *Nature Geoscience*, *15*(7), 520–530. https://doi.org/10.1038/s41561-022-00953-y

Li, X., Zhao, J., & Kwan, J. S. (2020). Assessing debris flow impact on flexible ring net barrier: A coupled CFD-DEM study. *Computers and Geotechnics*, *128*, 103850. https://doi.org/10.1016/j.compgeo.2020.103850

Li, X., Zhao, J., & Soga, K. (2021). A new physically based impact model for debris flow. *Géotechnique*, *71*(8), 674–685. https://doi.org/10.1680/jgeot.18.P.365

Liu, C., Yu, Z., & Zhao, S. (2020). Quantifying the impact of a debris avalanche against a flexible barrier by coupled DEM-FEM analyses. *Landslides*, *17*(1), 33–47. https://doi.org/10.1007/s10346-019-01267-8

Logan, M., Iverson, R. M., & Obryk, M. K. (2018). Video documentation of experiments at the USGS debris-flow flume 1992–2018. USGS Open-file Report. Retrieved from http://pubs.usgs.gov/of/2007/1315/

Ng, C. W. W., Song, D., Choi, C. E., Liu, L. H. D., Kwan, J. S. H., Koo, R. C. H., & Pun, W. K. (2017). Impact mechanisms of granular and viscous flows on rigid and flexible barriers. *Canadian Geotechnical Journal*, *54*(2), 188–206. https://doi.org/10.1139/cgj-2016-0128

Pasqua, A., Leonardi, A., & Pirulli, M. (2022). Coupling Depth-Averaged and 3D numerical models for the simulation of granular flows. *Computers and Geotechnics*, *149*, 104879. https://doi.org/10.1016/j.compgeo.2022.104879

Pisano, L., Zumpano, V., Malek, Ž., Rosskopf, C. M., & Parise, M. (2017). Variations in the susceptibility to landslides, as a consequence of land cover changes: A look to the past, and another towards the future. *Science of the Total Environment*, *601*, 1147–1159. https://doi.org/10.1016/j.scitotenv.2017.05.231

Piton, G., Goodwin, S. R., Mark, E., & Strouth, A. (2022). Debris flows, boulders and constrictions: A simple framework for modeling jamming, and its consequences on outflow. *Journal of Geophysical Research: Earth Surface*, *127*(5), e2021JF006447. https://doi.org/10.1029/2021JF006447

Potyondy, D. O., & Cundall, P. A. (2004). A bonded-particle model for rock. *International Journal of Rock Mechanics and Mining Sciences*, *41*(8), 1329–1364. https://doi.org/10.1016/j.ijrmms.2004.09.011

Pudasaini, S. P., & Fischer, J. T. (2020). A mechanical model for phase separation in debris flow. *International Journal of Multiphase Flow*, *129*, 103292. https://doi.org/10.1016/j.ijmultiphaseflow.2020.103292

Pudasaini, S. P., & Krautblatter, M. (2021). The mechanics of landslide mobility with erosion. *Nature Communications*, *12*(1), 6793. https://doi.org/10.1038/s41467-021-26959-5

Pudasaini, S. P., & Mergili, M. (2019). A multi-phase mass flow model. *Journal of Geophysical Research: Earth Surface*, *124*(12), 2920–2942. https://doi.org/10.1029/2019JF005204

Redaelli, I., di Prisco, C., & Calvetti, F. (2021). Dry granular masses impacting on rigid obstacles: Numerical analysis and theoretical modelling. *Acta Geotechnica*, *16*(12), 3923–3946. https://doi.org/10.1007/s11440-021-01337-z

Remaître, A., Malet, J. P., Maquaire, O., Ancey, C., & Locat, J. (2005). Flow behaviour and runout modelling of a complex debris flow in a clay-shale basin. *Earth Surface Processes and Landforms*, *30*(4), 479–488. https://doi.org/10.1002/esp.1162

Song, D., Bai, Y., Chen, X. Q., Zhou, G. G. D., Choi, C. E., Pasuto, A., & Peng, P. (2022). Assessment of debris flow multiple-surge load model based on the physical process of debris-barrier interaction. *Landslides*, *19*(5), 1165–1177. https://doi.org/10.1007/s10346-021-01778-3

Song, D., Choi, C. E., Ng, C. W. W., & Zhou, G. G. D. (2018). Geophysical flows impacting a flexible barrier: Effects of solid-fluid interaction. *Landslides*, *15*(1), 99–110. https://doi.org/10.1007/s10346-017-0856-1

Song, D., Choi, C. E., Ng, C. W. W., Zhou, G. G. D., Kwan, J. S., Sze, H. Y., & Zheng, Y. (2019). Load-attenuation mechanisms of flexible barrier subjected to bouldery debris flow impact. *Landslides*, *16*(12), 2321–2334. https://doi.org/10.1007/s10346-019-01243-2

Song, D., Zhou, G. G., Chen, X. Q., Li, J., Wang, A., Peng, P., & Xue, K. X. (2021). General equations for landslide-debris impact and their application to debris-flow flexible barrier. *Engineering Geology*, *288*, 106154. https://doi.org/10.1016/j.enggeo.2021.106154

Tan, D. Y., Yin, J. H., Feng, W. Q., Qin, J. Q., & Zhu, Z. H. (2018). Large-scale physical modelling study of a flexible barrier under the impact of granular flows. *Natural Hazards and Earth System Sciences*, *18*(10), 2625–2640. https://doi.org/10.5194/nhess-18-2625-2018

Tan, D. Y., Yin, J. H., Feng, W. Q., Zhu, Z. H., Qin, J. Q., & Chen, W. B. (2019). New simple method for calculating impact force on flexible barrier considering partial muddy debris flow passing through. *Journal of Geotechnical and Geoenvironmental Engineering*, *145*(9), 04019051. https://doi.org/10.1061/(ASCE)GT.1943-5606.0002133

Tan, D. Y., Yin, J. H., Qin, J. Q., Zhu, Z. H., & Feng, W. Q. (2020). Experimental study on impact and deposition behaviours of multiple surges of channelized debris flow on a flexible barrier. *Landslides*, *17*(7), 1577–1589. https://doi.org/10.1007/s10346-020-01378-7

Trottet, B., Simenhois, R., Bobillier, G., Bergfeld, B., Herwijnen, A., Jiang, C., & Gaume, J. (2022). Transition from sub-Rayleigh anticrack to supershear crack propagation in snow avalanches. *Nature Physics*, *18*(9), 1094–1098. https://doi.org/10.1038/s41567-022-01662-4

Vagnon, F., & Segalini, A. (2016). Debris flow impact estimation on a rigid barrier. *Natural Hazards and Earth System Sciences*, *16*(7), 1691–1697. https://doi.org/10.5194/nhess-16-1691-2016

Vicari, H., Ng, C. W., Nordal, S., Thakur, V., De Silva, W. R. K., Liu, H., & Choi, C. E. (2021). The effects of upstream flexible barrier on the debris flow entrainment and impact dynamics on a terminal barrier. *Canadian Geotechnical Journal*, *59*(6), 1007–1019. https://doi.org/10.1139/cgj-2021-0119

Vicari, H., Tran, Q. A., Nordal, S., & Thakur, V. (2022). MPM modelling of debris flow entrainment and interaction with an upstream flexible barrier. *Landslides*, *19*(9), 2101–2115. https://doi.org/10.1007/s10346-022-01886-8

Von Boetticher, A., Turowski, J. M., McArdell, B. W., Rickenmann, D., & Kirchner, J. W. (2016). DebrisInterMixing-2.3: A finite volume solver for three-dimensional debris-flow simulations with two calibration parameters – Part 1: Model description. *Geoscientific Model Development*, *9*(9), 2909–2923. https://doi.org/10.5194/gmd-9-2909-2016

Von Boetticher, A., Volkwein, A., Wüchner, R., Bletzinger, K. U., & Wendeler, C. (2011). Numerical modeling of shallow landslide impacts on flexible protection systems and its validation with full scale testing. In *COUPLED IV: Proceedings of the IV international conference on computational methods for coupled problems in science and engineering* (pp. 731–742). CIMNE. Retrieved from http://hdl.handle.net/2117/327389

Wang, L., Song, D., Zhou, G. G., Chen, X. Q., Xu, M., Choi, C. E., & Peng, P. (2022). Debris flow overflowing flexible barrier: Physical process and drag load characteristics. *Landslides*, *19*(8), 1881–1896. https://doi.org/10.1007/s10346-022-01880-0

Wendeler, C. (2016). Debris-flow protection systems for mountain torrents: Basics principles for planning and calculation of flexible barriers. *WSL Berichte*, *44*, 267.

Wendeler, C., Volkwein, A., McArdell, B. W., & Bartelt, P. (2019). Load model for designing flexible steel barriers for debris flow mitigation. *Canadian Geotechnical Journal*, *56*(6), 893–910. https://doi.org/10.1139/cgj-2016-0157

Xu, H., Gentilini, C., Yu, Z., Qi, X., & Zhao, S. (2018). An energy allocation-based design approach for flexible rockfall protection barriers. *Engineering Structures*, *173*, 831–852. https://doi.org/10.1016/j.engstruct.2018.07.018

Yu, T., & Zhao, J. (2021). Semi-coupled resolved CFD–DEM simulation of powder-based selective laser melting for additive manufacturing. *Computer Methods in Applied Mechanics and Engineering*, *377*, 113707. https://doi.org/10.1016/j.cma.2021.113707

Zhang, Z., Walter, F., McArdell, B. W., de Haas, T., Wenner, M., Chmiel, M., & He, S. (2021). Analyzing bulk flow characteristics of debris flows using their high frequency seismic signature. *Journal of Geophysical Research: Solid Earth*, *126*(12), e2021JB022755. https://doi.org/10.1029/2021JB022755

Zhao, J., & Shan, T. (2013). Coupled CFD–DEM simulation of fluid-particle interaction in geomechanics. *Powder Technology*, *239*, 248–258. https://doi.org/10.1016/j.powtec.2013.02.003

Zhao, T., & Crosta, G. B. (2018). On the dynamic fragmentation and lubrication of coseismic landslides. *Journal of Geophysical Research: Solid Earth*, *123*(11), 9914–9932. https://doi.org/10.1029/2018JB016378

Zheng, H., Shi, Z., de Haas, T., Shen, D., Hanley, K. J., & Li, B. (2022). Characteristics of the impact pressure of debris flows. *Journal of Geophysical Research: Earth Surface*, *127*(3), e2021JF006488. https://doi.org/10.1029/2021JF006488

Zhou, G. G., Cui, K. F., Jing, L., Zhao, T., Song, D., & Huang, Y. (2020). Particle size segregation in granular mass flows with different ambient fluids. *Journal of Geophysical Research: Solid Earth*, *125*(10), e2020JB019536. https://doi.org/10.1029/2020JB019536

References From the Supporting Information

Di Felice, R. (1994). The voidage function for fluid-particle interaction systems. *International Journal of Multiphase Flow*, *20*(1), 153–159. https://doi.org/10.1016/0301-9322(94)90011-6

Geobrugg, A. G. (2012). Geobrugg: Barreras contra flujos de detritus. Retrieved from https://www.youtube.com/watch?v=hMu9VAEGe1A

Shan, T., & Zhao, J. (2014). A coupled CFD-DEM analysis of granular flow impacting on a water reservoir. *Acta Mechanica*, *225*(8), 2449–2470. https://doi.org/10.1007/s00707-014-1119-z

Zhou, Z. Y., Kuang, S. B., Chu, K. W., & Yu, A. B. (2010). Discrete particle simulation of particle-fluid flow: Model formulations and their applicability. *Journal of Fluid Mechanics*, *661*, 482–510. https://doi.org/10.1017/S002211201000306X